Influence of Graphene Thickness and Grain Boundaries on MoS_2 Wrinkle Nanostructures

Journal:	*Physical Chemistry Chemical Physics*
Manuscript ID	CP-ART-04-2018-002460.R1
Article Type:	Paper
Date Submitted by the Author:	24-May-2018
Complete List of Authors:	Kim, Seon Joon; Korea Advanced Institute of Science and Technology, Department of Chemical and Biomolecular Engineering Kwon, Ohmin; Korea Advanced Institute of Science and Technology Kim, Dae Woo; Korea Advanced Institute of Science and Technology, Department of Chemical and Biomolecular Engineering Kim, Jihan; KAIST, Chemical and Biomolecular Engineering Jung, Hee-Tae; Korea Advanced Institute of Science and Technology, Department of Chemical + Biomolecular Engineering

PCCP

ARTICLE

Influence of Graphene Thickness and Grain Boundaries on MoS_2 Wrinkle Nanostructures

Received 00th January 20xx,
Accepted 00th January 20xx

DOI: 10.1039/x0xx00000x

www.rsc.org/

Seon Joon Kim [a], Ohmin Kwon [b], Dae Woo Kim [a], Jihan Kim [b, c], Hee-Tae Jung *[, a, c]

Controlling wrinkle nanostructures of two-dimensional materials is critical for optimizing the material properties and device performance. In this study, we demonstrated the *in situ* synthesis of large-area MoS_2 wrinkles on graphene by chemical-vapor-deposition-assisted sulfurization, and investigated the influence of graphene thickness and grain structures on the feature dimensions of MoS_2 wrinkle nanostructures. The height, width, and overall surface roughness of the MoS_2 wrinkles diminish as the number of graphene layers increases, which was further verified by determining the binding energy of graphene layers by density functional theory calculations. Furthermore, the feature dimensions of MoS_2 wrinkle nanostructures were also influenced by graphene domain boundaries because of the difference in graphene nucleation density. This may be attributed to the influence of the mechanical properties of graphene substrates on the overall feature dimensions of MoS_2 wrinkles, which are directly correlated with the interfacial adhesion energy. We believe that our findings may contribute toward the controllable synthesis of MoS_2 wrinkle nanostructures and other two-dimensional materials used for high-performance devices.

1. Introduction

Mechanical instability at the interface of two different layers causes the formation of wrinkles or ridges, which relieves the residual stress in a film[1–3]. Wrinkles in nanomaterials offer a wide range of advantages for controlling the surface properties of thin films, such as surface adhesion[4–6], wettability[7,8], as well as for enhancing the performance of sensors[9,10], photovoltaics (such as organic solar cells)[11], and organic light-emitting diodes[12]. Moreover, the structural morphology of wrinkles has been used to align nanowires[13] and block copolymers[14] over a long range. It is well known that controlling the nanostructures of two-dimensional (2D) materials generates favorable properties[15-17]. Accordingly, wrinkle fabrication has been recently extensively applied to 2D materials. For example, wrinkled graphene films display enhanced optoelectrical efficiency in plasmonic sensors based on surface-enhanced Raman scattering[18] and in photodetectors[19]. Graphene and MoS_2 wrinkles have been employed as high-performance platforms for energy storage[20] and electrocatalysis[21], respectively. Furthermore, optimized performance in biological applications was achieved by the precise control of wrinkle dimensions. For instance, the antibacterial activity of wrinkled graphene oxide (GO) films was the highest when the GO wrinkle roughness was made closer to the bacterial diameter[22]. The highest activity in stem cell differentiation was observed on nanocrystalline graphitic films with the highest percentage of wrinkles[23].

Although various techniques are available for the synthesis of wrinkle nanostructures in 2D materials, only a few allow scalable control over wrinkle dimensions. First, the most common and accessible method for the synthesis and control of the wrinkle nanostructure of 2D materials is the deposition of 2D films on pre-strained elastomeric substrates[24-26], which has been employed to synthesize graphene and MoS_2 wrinkles. In this method, wrinkles are synthesized by relieving the strain in pre-strained substrates. The wrinkle dimensions are manipulated by controlling the intensity and axial direction of contraction during strain relief. A second approach for forming wrinkles in 2D materials is tuning the surface tension of the transfer media[27]. Previous studies have shown that graphene sheets floating on water can be shrunk when transferred onto a water/ethanol mixture because of the reduced surface tension of the solution. In this method, wrinkle dimensions are simply controlled by adjusting the ethanol concentration. In a third technique, wrinkles are synthesized by integrating 2D materials onto pre-featured substrates[28]. In this method, control over wrinkle dimensions can be achieved by tuning substrate architecture; however, the method lacks scalability because of its elaborate process.

[a] National Research Laboratory for Organic Opto-Electronic Materials, Department of Chemical and Biomolecular Engineering (BK-21 Plus), Korea Advanced Institute of Science and Technology (KAIST), Daejeon 34141, South Korea.
[b] Department of Chemical and Biomolecular Engineering (BK-21 Plus), South Korea Advanced Institute of Science and Technology (KAIST), Daejeon 34141, South Korea
[c] KAIST Institute for Nanocentury, Korea Advanced Institute of Science and Technology (KAIST), Daejeon 34141, South Korea.

† Electronic Supplementary Information (ESI) available: See DOI: 10.1039/x0xx00000x

Herein, we prepared controlled nanostructures of MoS_2 wrinkles over a large area by sulfurization of Mo precursor films on graphene grown by chemical vapor deposition (CVD)-. Ridge-like MoS_2 wrinkles were synthesized *in situ* during sulfurization, unlike in conventional methods in which post-synthesis processes are employed to synthesize wrinkles. We found that the graphene thickness and graphene domain boundaries play a significant role in determining the feature dimensions of MoS_2 wrinkles: tuning the number of graphene layers allowed the controlled synthesis of MoS_2 wrinkle nanostructures. To resolve the overall mechanism behind the control of MoS_2 wrinkle feature dimensions, the mechanical properties of graphene substrates were theoretically correlated with the interfacial adhesion energy, which was then compared with the experimental results. Furthermore, the adhesion energy of each graphene substrate was calculated by density functional theory (DFT) to support the theoretical correlations.

2. Experimental Methods

2.1. Preparation and transfer of monolayer and few-layer graphene

Cu foil pieces (25 μm thickness, Goodfellow) were placed in a 4-inch-diameter quartz tube in a chemical vapor deposition apparatus. H_2 at 8 sccm was introduced into a vacuum environment, and the chamber was heated to 1040°C for 1 hour. The carbon source, CH_4 at 50 sccm, was introduced for 10 minutes at a constant temperature to grow graphene. The furnace was rapidly cooled to room temperature while only H_2 flow was retained in the chamber. For the transfer process, graphene was coated with a poly(methyl methacrylate) (PMMA) support by spin coating and then annealed at 180°C to remove residual solvents. Cu was then dissolved using an iron(III) chloride ($FeCl_3$) solution, and the PMMA–graphene film was washed with distilled water before it was transferred onto a SiO_2 substrate. The PMMA layer was dissolved in acetone to expose the graphene film. Transfer cycles were repeated several times on a single target substrate for the preparation of bilayer, trilayer, and tetralayer graphene.

Graphene islands for the observation of nuclei were prepared by limiting the CH_4 injection duration to less than 30 seconds. For the clear observation of graphene nuclei, Cu foil samples with graphene islands were briefly heated at 200°C in air to oxidize the bare surface of uncovered Cu.

2.2 Preparation and transfer of graphite

Ni foil pieces (25 μm thickness, Goodfellow) were placed in a 4-inch-diameter tube, and then H_2 at 50 sccm and Ar at 300 sccm were introduced into the chamber. The total pressure inside the chamber was kept at 10 Torr while the temperature was elevated to 1040°C for 1 hour. CH_4 at 50 sccm was introduced for 20 minutes at a constant temperature to supply a carbon source for the Ni bulk. The furnace was rapidly cooled to room temperature to complete graphite growth. Prior to the transfer process, graphite grown on the back side of the Ni foil was etched with plasma so that only graphite from the front side was used. The remaining transfer processes of CVD-grown graphite films were the same method as that used for monolayer graphene.

2.3. Observation of graphene domains

4-Cyano-4′-pentylbiphenyl (5CB) was spin coated onto graphene transferred to SiO_2 substrates in order to fabricate a uniform liquid crystal thin film. Polarized optical microscopy (POM) was used to observe the graphene domains at room temperature (25°C), and a lambda plate was utilized to obtain color images.

2.4. Theoretical methods for calculating adhesion energy

DFT calculations were conducted using the Quantum-Espresso program[29]. The initial structure of reconstructed SiO_2 system was obtained from a previous work[30]. The initial unit cell of graphene was expanded to match the lattice parameters of the SiO_2 within a single unit cell. In the case of graphene with SiO_2 system, graphene was put on top of the SiO_2 surface and fully relaxed. There is a small lattice mismatch of less than 5% in the total unit cell due to different cell parameters between the SiO_2 and the graphene system. A vacuum spacing of more than 15 Å was used to avoid the artificial interaction between the cells. The 7 × 7 × 1 Monkhorst–Pack k-point grids[31] were used in the calculation of graphene/SiO_2 systems, and the 7 × 7 × 5 grids were used in calculation of bulk graphite systems. The planewave kinetic energy cutoff for wavefunctions was set to 60 Ry (≒ 816 eV).

All of the energies are obtained from single point energy calculations and the adhesion energy was calculated using the following formulas:

$$\Delta E_{SiO_2-graphene} = (E_{Graphene\ with\ SiO_2} - (E_{Monolayer\ graphene} + E_{SiO_2}))/Area$$

$$\Delta E_{G-G\ (Bilayer)} = (E_{Bilayer\ graphene} - 2 \times E_{Monolayer\ graphene})/Area$$

$$\Delta E_{G-G\ (Graphite)} = (E_{Graphite} - N \times E_{Monolayer\ graphene})/Area$$

(N: number of graphene layers in a graphite unit cell)
(G: graphene layers)

2.5. Equipment and characterization

The surface morphologies of graphene were analyzed using scanning electron microscopy (SEM, FEI Nova230), and topologies were measured using atomic force microscopy (AFM, Park Systems). Cross-sectional images were prepared by a focused ion beam (FEI Helios Nanolab 450 F1) and then observed by transmission electron microscopy (TEM, FEI Tecnai TF30 ST). The film properties of MoS_2 and graphene were also analyzed by Raman spectroscopy (Horiba Jobin Yvon ARAMIS), and grazing-incidence X-ray diffraction experiments were conducted at the Pohang Accelerator Laboratory (Pohang, Korea) using a beam size of 200 μm × 500 μm (Rayonix 2D MAR 165 detector). Liquid-crystal-coated graphene layers were observed under a polarized optical microscope (Nikon).

3. Results and Discussion

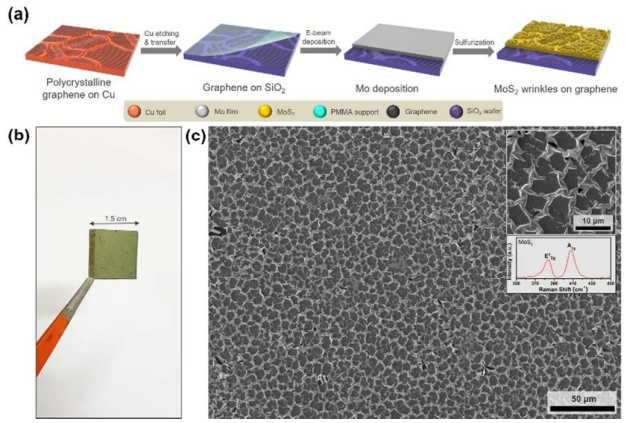

Figure 1. Synthesis of large-area MoS_2 wrinkles on graphene. (a) Schematic illustration for synthesizing MoS_2 wrinkles on graphene. Polycrystalline graphene is grown by LPCVD on Cu, which is then transferred onto a SiO_2 substrate. The Mo precursor films are then deposited by e-beam deposition and then sulfurized into MoS_2 *via* CVD. (b) Image of MoS_2 wrinkles synthesized on a 1.5 × 1.5 cm^2 SiO_2 wafer. (c) Large-area and magnified (top inset) SEM images of synthesized MoS_2 wrinkles. The bottom inset shows the Raman spectrum of the MoS_2 wrinkled films.

The schematic illustration for fabricating MoS_2 wrinkle nanostructures on graphene is displayed in **Fig. 1a**. Initially, monolayer graphene was grown on a Cu foil *via* low-pressure chemical vapor deposition (LPCVD) at an elevated temperature (1040°C). Because of the polycrystalline nature of the Cu catalyst substrate, graphene films with polycrystalline domain structures were obtained[32]. The graphene then was transferred onto pre-cleaned SiO_2/Si substrates by a conventional wet-transfer method with a PMMA support film. Transfer steps were repeated multiple times on a single substrate in order to obtain few-layer graphene films. The Raman spectrum of a transferred film was obtained in order to investigate the quality of graphene films (**Fig. S1**). A negligible D peak at 1355 cm^{-1} and a small I_D/I_G (intensity of D peak over that of G peak) ratio of 0.08 can be observed; these indicate the successful transfer of high-quality graphene films with few defects[33]. Afterward, a molybdenum (Mo) precursor film of 20 nm thickness was deposited on the graphene film *via* e-beam deposition. For the next step, Mo films on graphene were further converted to MoS_2 by rapid sulfurization *via* CVD. Here, a two-chamber setup was used to precisely control the operation temperature. Excess amounts of sulfur (S_8) powders were placed in the upstream chamber to ensure complete sulfurization, while the Mo deposited graphene substrates were placed in the downstream chamber. The temperature of the downstream chamber with Mo-graphene substrates was elevated to 770 °C under an Ar atmosphere, and the temperature of the upstream chamber with sulfur powders was elevated to 220 °C to begin sulfurization. Sulfurization was performed at 770 °C for 20 minutes, and then the chamber was cooled down to room temperature to complete the conversion of Mo films to MoS_2. The synthesized films consisted of edge-oriented MoS_2 layers (**Fig. S2**), while the underlying graphene layer induced buckling of the MoS_2 film, creating wrinkles[21].

Since MoS_2 wrinkles were directly synthesized over the CVD-grown graphene substrate, wrinkles were synthesized over a very large area. **Fig. 1b** shows a photographic image of MoS_2 wrinkles synthesized on a 1.5 × 1.5 cm^2 SiO_2/Si substrate. Here, the light-scattering effect of wrinkles resulted in a matte surface. The SEM image in **Fig. 1c** shows that uniform wrinkles were present over a large area; the morphology of individual wrinkles is shown in the magnified SEM image in the top inset. Furthermore, the Raman spectrum of the synthesized MoS_2 film in the bottom inset of **Fig. 1c** displays two sharp peaks at 383 and 409 cm^{-1}, which correspond to the E^1_{2g} and A_{1g} peaks of MoS_2[34]; these indicate the synthesis of high-quality films.

Fig. 2 shows the change in MoS_2 wrinkled nanostructures as a function of graphene thickness. The graphene thickness was controlled by sequential transfer of monolayer graphene grown on Cu onto SiO_2 substrates, from which monolayer, bilayer, trilayer, and tetralayer graphene substrates were fabricated. The increasing number of graphene layers can be clearly seen in the Raman spectra (**Fig. S3**). Here, the intensity ratio (I_G/I_{2D}) of the G peak at 1586 cm^{-1} to the 2D peak at 2690 cm^{-1} gradually increases from 0.7 (monolayer) to 1.5 (tetralayer). The low intensity of the D peak at 1355 cm^{-1} also indicates high-quality graphene layers with few defects. Mo films of 20 nm thickness were then deposited on few-layer graphene and then converted into MoS_2 wrinkles by rapid sulfurization *via* CVD. We found that the feature dimensions of wrinkle nanostructures were significantly different in terms of the underlying graphene thickness. **Fig. 2a–d** shows that the largest wrinkles formed on monolayer graphene, while the feature dimensions of wrinkles gradually diminished as the graphene substrate became thicker. AFM measurements of each sample were conducted to precisely measure the feature dimensions of wrinkles, as shown in **Fig. 2e–h**. The average MoS_2 wrinkle heights were 0.86, 0.65, 0.39, and 0.28 μm on mono-, bi-, tri-, and tetralayer graphene, respectively, while the average MoS_2 wrinkle widths were 1.16, 0.49, 0.16, and 0.14 μm, respectively; this result shows the gradual decrement in MoS_2 wrinkle dimensions. The wrinkle density gradually also increased as the graphene substrate became thicker, as seen in the images. The surface roughness was also measured by calculating the surface area increment. The total increments relative to the geometric area were 20.4%, 15.3%, 14.3%, and 13.4% for MoS_2 synthesized on mono-, bi-, tri-, and tetralayer graphene, respectively (summarized in **Fig. 2i**). The overall trend clearly shows that the feature dimensions of MoS_2 wrinkled nanostructures gradually diminish as the graphene substrate becomes thicker. To further confirm this correlation, MoS_2 was synthesized on CVD-grown graphite corresponding to approximately 300 layers of turbostratically stacked graphene layers. **Fig. S4** shows that after the growth of MoS_2 on the graphite substrate, MoS_2 wrinkles became unobservable, coinciding with the observed trend of diminishing wrinkles for thicker graphene substrates.

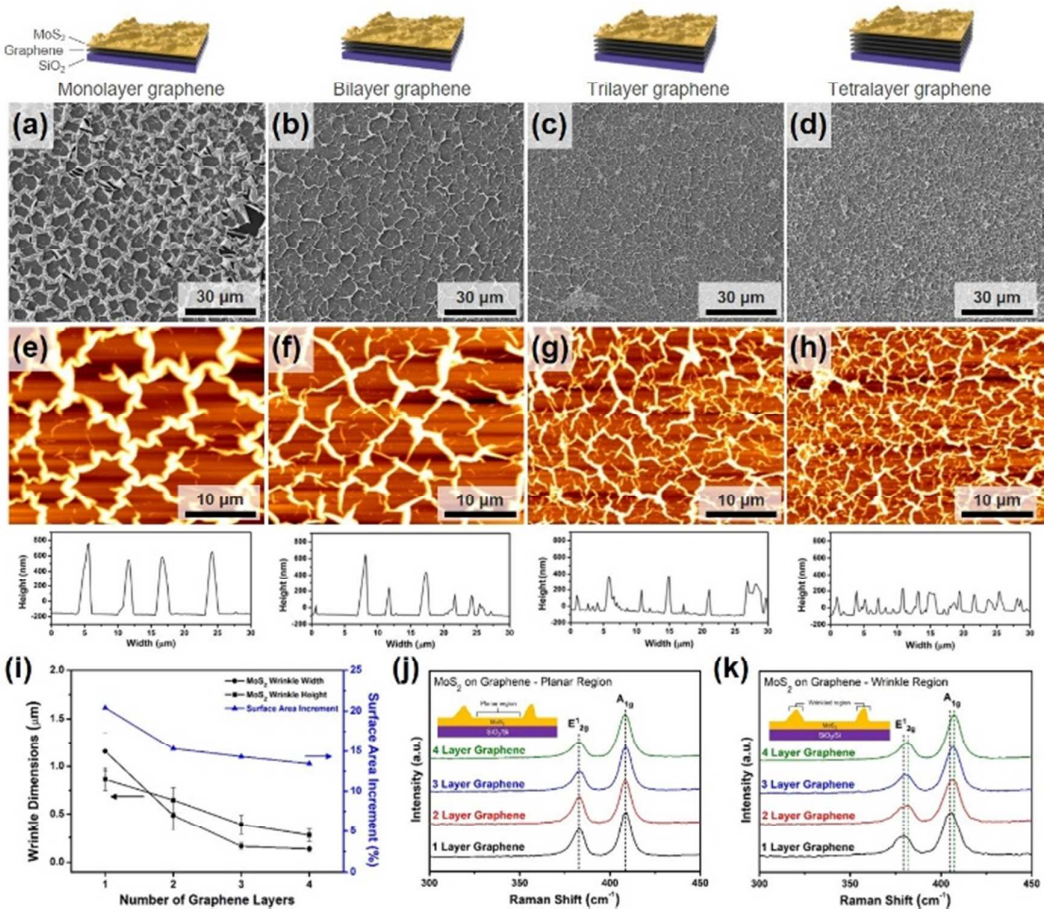

Figure 2. Influence of the graphene thickness on the feature dimensions of MoS_2 wrinkles. (a–d) SEM images of large-area MoS_2 wrinkles synthesized on (a) monolayer, (b) bilayer, (c) trilayer, and (d) tetralayer graphene. (e–h) AFM images of MoS_2 wrinkles synthesized on (e) monolayer, (f) bilayer, (g) trilayer, and (h) tetralayer graphene. Graphs under each AFM image display representative height profiles. (i) Correlation of the number of graphene layers with the MoS_2 wrinkle dimensions (left, black) and surface area increment relative to the geometric area (right, blue). (j, k) Raman spectra of MoS_2 films on graphene at the (j) planar region and (k) wrinkle region. Insets in (j) and (k) represent the probed area.

In order to measure the residual stress in the wrinkles, the Raman spectra of MoS_2 synthesized on different layers of graphene were recorded, as shown in **Fig. 2j** and **k**. Interestingly, the peak positions of planar regions in MoS_2 films differed from those of wrinkled regions. Peak positions from a basal plane for all samples appeared at 383 and 409 cm^{-1}, which correspond to the E^1_{2g} and A_{1g} peaks of MoS_2; the peak positions obtained for the MoS_2 wrinkles on monolayer graphene red-shifted to 379 and 405 cm^{-1}. This type of peak shift indicates the presence of local stress in MoS_2 wrinkles[35], which typically appears on various types of wrinkled nanostructures. The peak shift gradually diminished for MoS_2 on thicker graphene substrates; the peak positions of MoS_2 wrinkles on tetralayer graphene appeared at 383 and 409 cm^{-1} with no peak shift. The above results indicate that the feature dimensions of MoS_2 wrinkled nanostructures can be controlled by changing the thickness of the underlying graphene substrate. In other words, tunable MoS_2 wrinkle growth can be achieved on graphene with controlled thickness. To demonstrate tunable MoS_2 wrinkle growth, varying layers of mono-, bi-, tri-, and tetralayer graphene were prepared on a single SiO_2 substrate, and then MoS_2 wrinkles were synthesized accordingly. **Fig. S5** shows that the synthesis of MoS_2 wrinkles with tunable feature dimensions at the desired regions, which can be precisely controlled through lithographic techniques.

In order to verify the adhesion energies of the graphene layers, we carried out DFT calculations. The interfacial adhesion energy largely influences the feature dimensions of wrinkles formed by buckle delamination, that is, weaker adhesion leads to larger wrinkles. Because of this phenomenon, the influence of graphene thickness on the feature dimensions of MoS_2 wrinkles was verified by calculating the interfacial adhesion energy of few-layer graphene sheets *via* DFT. Here, three different graphene models were investigated: monolayer graphene on SiO_2, bilayer graphene, and bulk graphite. For the case of monolayer graphene with SiO_2, a single configuration was used for calculation, as previous works have shown that the difference of binding energies from various positions of graphene on SiO_2 was small[36]. For bilayer graphene, the binding energy of freestanding graphene sheets without a SiO_2 layer and that of

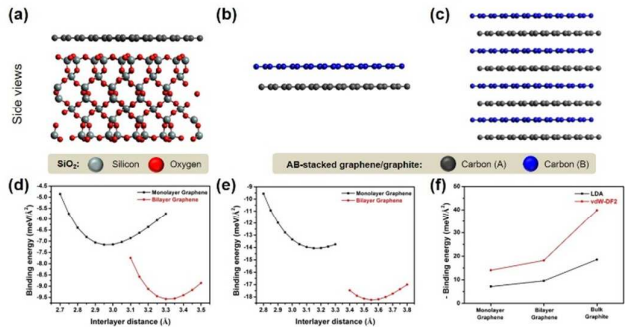

Figure 3. DFT calculations for the adhesion energies of various graphene layers. (a–c) Layer configurations of (a) monolayer graphene on SiO_2, (b) bilayer graphene, and (c) bulk graphite. α-Quartz was used for the SiO_2 layer, and the number of graphene unit cells in the *xy* direction was chosen to match the size of the SiO_2 unit cell. Graphene sheets were assumed to be AB-stacked. (d, e) Binding energies obtained from single point energy calculations according to various interlayer distances using (d) LDA and (e) vdW-DF2 for monolayer graphene (black) and bilayer graphene (red). (f) Minimum binding energies of monolayer graphene, bilayer graphene, and bulk graphite calculated using LDA and vdW-DF2.

graphene sheets on SiO_2 were nearly identical. Therefore, the values documented here were obtained from freestanding bilayer graphene without a SiO_2 layer. Two different functionals were used to calculate the exchange-correlation term, as shown in **Fig. 3** and **Table S1**: local density approximation (LDA)[37] and vdW-DF2[38] (used to calculate the van der Waals interaction term more accurately). For the initial calculations, α-quartz was used to represent the SiO_2 layer, and AB-stacked graphene was employed, which is the most stable state among various stacking orientations. **Fig. 3a–c** displays the side views of the unit cell of each model, and **Fig. S6** presents top views of the unit cell. The primitive cell of graphene was expanded to 2 x 2 in the *xy* direction to match the size of the SiO_2 unit cell. In order to determine the stable state of each model, binding energies were calculated by using single point energy calculations for various interlayer distances at a 0.5 Å interval. Here, the stable interlayer distance was obtained from the interlayer distance with the lowest binding energy (**Fig. 3d** and **e**). As a result, the stable interlayer distance between monolayer graphene and SiO_2 was 2.95 Å for LDA and 3.15 Å for vdW-DF2, and the stable distance between graphene layers in bilayer graphene was 3.30 Å for LDA and 3.55 Å for vdW-DF2. In both cases, the vdW-DF2 function displayed a larger interlayer distance compared with LDA. After relaxation, the stable interlayer distance in bulk graphite was 3.31 Å for LDA and 3.52 Å for vdW-DF2, similar to the empirical value of 3.35 Å. As shown in **Fig. 3f**, The LDA-based minimum binding energies of monolayer graphene with SiO_2, bilayer graphene, and bulk graphite were −7.15, −9.57, and −18.61 meV/Å^2, respectively, while vdW-DF2 calculations showed a similar trend; binding energies were −14.05 (mono-), −18.24 (bi-), and −39.80 meV/Å^2 (bulk). These results show that the binding strength increases as the number of graphene layers increases. That is, bulk graphite has double the binding energy for monolayer graphene, according to previous studies on graphitic binding energies.

In fact, the bilayer graphene used in experiments is closer to turbostratic graphene rather than AB-stacked graphene as they were prepared by sequential transfer of polycrystalline monolayer graphene. To obtain an estimate of the binding energy of such turbostratic graphene, we also calculated the binding energy of AA-stacked double-layer graphene, as previous works[39] have shown that the binding energy of turbostratic graphene lies in between those of AA- and AB-stacked graphene. As shown in **Table S2**, the minimum binding energy of AA-stacked bilayer graphene was -16.00 meV/Å^2. Thus, we can expect that turbostratic double-layer graphene will have a binding energy in between -16.00 and -18.24 meV/Å^2. Still, the entire range of binding energy for double-layer graphene is still above that of monolayer graphene (-14.05 meV/Å^2), which suggests that values calculated for turbostratic graphene will still follow the trend of increasing adhesion for thicker graphene films. In overall, DFT calculations indicate that the interfacial adhesion energy increases for thicker graphene substrates, in agreement with the experimental results for smaller MoS_2 wrinkles synthesized on thicker graphene substrates.

Interestingly, we found that the graphene domain boundaries also influenced the feature dimensions of MoS_2 wrinkled nanostructures. To directly observe the correlation between graphene domain structures and MoS_2 wrinkles, both features were directly compared in the same region. In order to fully grow Cu grains for clear comparison, Cu substrates were annealed at 1040°C for 1 h prior to graphene growth[40,41]. Pristine Cu substrates displayed a random grain orientation, while annealed substrates predominantly consisted of low-index crystal facets with a few high-index crystal facets in the form of twin crystals (see **Fig. S7**). The Cu grains became larger after annealing; the average grain sizes of pristine grains and those after annealing for 1 h were 8.3 and 150 μm, respectively. After annealing, monolayer graphene was grown by LPCVD and then transferred onto a SiO_2/Si substrate. In order to directly visualize the graphene domain structure over a large area, graphene films were spin-coated with a nematic liquid crystal (5CB) layer. The graphene quasi-domain boundaries were observed by the optical birefringence of the aligned liquid crystals[32]; this is shown in the POM image in **Fig. 4a**. Graphene domains synthesized on high-index Cu crystal facets significantly differed from those synthesized on low-index Cu crystal facets, as evident from the difference in the color-indicated degree of rotation of liquid crystal molecules. After the removal of liquid crystals, MoS_2 was sequentially synthesized on the graphene film (**Fig. 4a**). The optical image in **Fig. 4b** shows that MoS_2 wrinkles with a pattern identical to that of the graphene quasi-domain structure formed; this formation implies that the quasi-domain structure significantly influences the feature dimensions of MoS_2 wrinkles. Magnified images in the highlighted region (dotted box) of **Fig. 4b** obtained by SEM (shown in **Fig. 4c**) clearly display a difference in the wrinkle feature dimensions at the Cu crystal domain boundary. For quantitative

comparison, wrinkle dimensions of both sides of the grain boundary were measured by AFM, as shown in **Fig. S8**. The average width and height of MoS_2 wrinkles originating from a high-index Cu crystal facet region were 2.02 and 1.18 µm respectively, while those for wrinkles from a low-index facet region were 1.16 and 0.86 µm respectively; this result shows that wrinkles with larger feature dimensions formed on graphene grown on high-index Cu crystal facets.

the SEM image of graphene islands at the boundary between high-index and low-index Cu crystal facets. The graphene islands are clearly seen as black dots. Cu surfaces were slightly oxidized prior to SEM observation to clearly distinguish individual graphene islands. The surface image shows that the graphene nucleation density was substantially higher on high-index Cu facets in comparison with that on low-index Cu facets. We expected that the variation in graphene nucleation

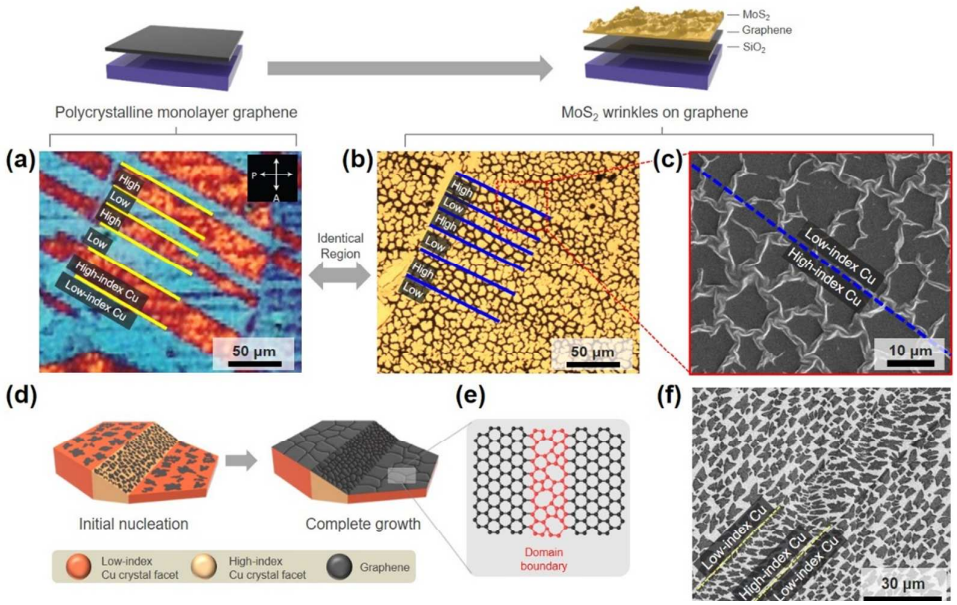

Figure 4. Influence of graphene domain boundaries on the feature dimensions of MoS_2 wrinkles. (a) POM image of polycrystalline monolayer graphene coated with 5CB liquid crystal, revealing the graphene quasi-domain boundaries. (b) Optical image of MoS_2 wrinkles synthesized on the region in (a). (c) SEM image of the highlighted region in (b), where the boundary of Cu crystal facets is indicated. (d, e) Schematic illustration of the (d) graphene nucleation on distinct Cu crystal facets and of (e) stitched graphene domain boundaries. (f) SEM image of graphene nucleation on Cu after 30 seconds of CVD growth. High-index Cu crystal facets displayed a graphene nucleation density higher than that of low-index Cu crystal facets.

We assumed that the difference in feature dimensions of MoS_2 wrinkles on distinct graphene quasi-domains is due to the difference in mechanical strength of each quasi-domain with the same film thickness. Such mechanical strength of a quasi-domain is largely influenced by the internal density of graphene domain boundaries, which is in turn influenced by the initial nucleation density of graphene[42]. Therefore, we investigated the difference in initial graphene nucleation behavior on distinct quasi-domains to estimate the variation in mechanical strength. The correlation between initial nucleation and graphene domain boundary is illustrated in **Fig. 4d** and **e**. Initially, carbon precursors rapidly bind to the Cu surface to initiate nucleation, which then laterally expands, resulting in fully growth of graphene across the entire surface (**Fig. 4d**). As the lattice parameters of graphene do not completely match those of Cu[43], graphene domain boundaries form at each stitching site despite similar lattice orientation (**Fig. 4e**). The number of domain boundaries is proportional to the initial nucleation density.

In order to experimentally observe the initial graphene nucleation behavior, methane was briefly included to partially grow graphene islands on polycrystalline Cu. **Fig. 4f** displays

density for distinct crystal facets is due to the different binding energies of graphene precursors to each Cu facet[44]. Previous studies have shown that Cu surfaces with a high-index crystal facet possess a precursor adsorption energy higher than that of low-index crystal facets, leading to favored graphene growth on high-index Cu facets[45]. From these results, we can deduce that a higher density of graphene domain boundaries exists on high-index Cu crystal facets after graphene growth is complete. On the basis of our empirical results, we can conclude that a higher density of graphene domain boundaries leads to more severe buckling, leading to larger MoS_2 wrinkles.

To further verify the influence of graphene domains on MoS_2 wrinkle feature dimensions, MoS_2 wrinkles were synthesized on arbitrary graphene quasi-domains and compared. **Fig. S9** shows the nucleation behavior of graphene in an arbitrary region of polycrystalline Cu, and **Fig. S10** shows the correlation between feature dimensions of MoS_2 wrinkles with graphene quasi-domain structure in an arbitrary region. **Fig. S9** indicates that the graphene nuclei density clearly differs on all Cu crystal facets. According to our assumption, such a universal difference may lead to distinct MoS_2 wrinkle dimensions in all regions and not only between high-index and

low-index Cu crystal facets. We can indeed observe in **Fig. S10** that the pattern of MoS_2 wrinkles is identical to that of graphene quasi-domains in an arbitrary region, and that the MoS_2 wrinkle dimensions are significantly distinct in all regions. These results support our assumption that the graphene domain boundaries play a significant role in determining the feature dimensions of MoS_2 wrinkles.

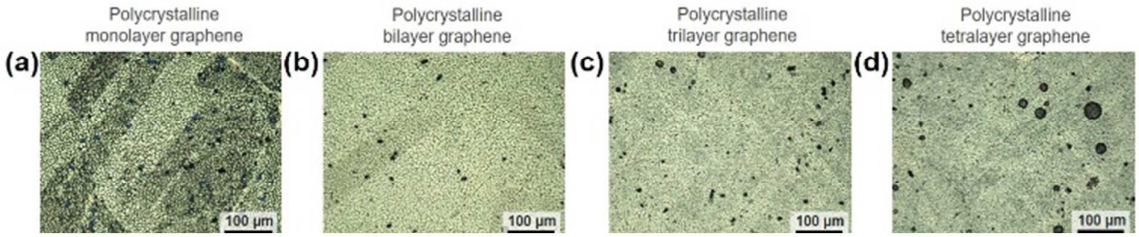

Figure 5. Influence of graphene domain boundaries on the feature dimensions of MoS_2 wrinkles synthesized on few-layer graphene. (a–d) Surface images of MoS_2 wrinkles on (a) monolayer, (b) bilayer, (c) trilayer, and (d) tetralayer graphene. The influence of the graphene domain on the feature dimensions of MoS_2 wrinkles weakens as graphene becomes thicker.

As a result, the MoS_2 wrinkle feature dimensions are influenced by the graphene thickness and the density of graphene domain boundaries. Both parameters were correlated with the interfacial adhesion energy, which is influenced by mechanical properties. The interfacial adhesion energy (Γ) is known to be proportional to the stretching stiffness (E_{2D}) and the bending stiffness (D) of a buckled film[46]. It is expressed as the following equation:

$$\Gamma = k_1 \cdot E_{2D} + k_2 \cdot D$$

where k_1 and k_2 are values dependent on the wrinkle dimensions.

First, the influence of graphene thickness in **Fig. 2** was correlated with the bending stiffness (D) of graphene. Previous studies have shown that the bending stiffness of graphene sheets drastically increases as the number of layers increases; the stiffness of tetralayer graphene (D = 12.50 eV) is an order of magnitude higher than that of monolayer graphene (D = 1.5 eV) [47]. Because stretching stiffness is similar for monolayer and few-layer graphene[48], we can deduce from the equation that the adhesion energy of few-layer graphene is considerably higher than that of monolayer graphene. Second, the influence of the graphene domain boundaries in **Fig. 4** was correlated with the stretching stiffness (E_{2D}) of graphene. Graphene domain boundaries have mechanical strength lower than that of basal planes; indentation experiments have directly shown that graphene with a low density of domain boundaries possess mechanical strength (E_{2D} = 339 N/m) higher than that of graphene with a high density of domain boundaries (E_{2D} = 328 N/m) [49]. Assuming a similar bending strength for both types due to similar layer thickness, we can deduce from the equation that the adhesion energy of graphene with a higher density of grain boundaries is lower than that with large grains, eventually leading to larger MoS_2 wrinkles.

The equation above also implies that graphene domain boundaries influence the feature dimensions of MoS_2 wrinkles on both monolayer and few-layer graphene. **Fig. 5** shows optical images of MoS_2 wrinkles synthesized on polycrystalline mono, bi-, tri-, and tetralayer graphene. These show that the distinct MoS_2 wrinkles along the graphene quasi-domain pattern are clearly distinguishable on the monolayer graphene, while the difference slowly fades with thicker graphene substrates. This phenomenon can be explained by the equation above; the second term ($k_2 \cdot D$) becomes much larger for few-layer graphene ($D_{4LG}/D_{1LG} \fallingdotseq 8$), becoming the dominant term that determines the overall interfacial adhesion energy.

4. Conclusions

In conclusion, we synthesized and controlled MoS_2 wrinkle nanostructures on various graphene substrates through rapid sulfurization via CVD, and investigated the major factors influencing the feature dimensions of wrinkles. We demonstrated large influence of the graphene thickness and density of graphene domain boundaries on the feature dimensions of MoS_2 wrinkles. MoS_2 wrinkles on few-layer graphene gradually diminished as the graphene thickness increased; the wrinkles were not observed at all on thick graphite, and the controlled growth of MoS_2 wrinkles was achieved by precisely tuning the number of graphene layers prior to sulfurization. DFT calculations further support the influence of graphene thickness, revealing that the adhesion energy increased as the graphene substrate became thicker. We correlated the feature dimensions of MoS_2 wrinkles with the mechanical properties of graphene substrates. Here, we showed the contributions of graphene thickness and domain boundaries to the overall interfacial adhesion energy. We expect that our finding will pave a way toward tunable morphology control of MoS_2 and other 2D materials for enhanced properties and device performance.

Conflicts of interest

There are no conflicts to declare.

Acknowledgements

This work was supported by the National Research Foundation of Korea (NRF), funded by the Ministry of Science, ICT, and Future Planning, Korea (MSIP, Grant No. 2015R1A2A1A05001844), Global Frontier Research Center for Advanced Soft Electronics (No. 2014M3A6A5060937, MSIP),

and the Climate Change Research Hub of KAIST (No. N1117056). This research used resources of the National Energy Research Scientific Computing Center, a DOE Office of Science User Facility supported by the Office of Science of the U.S. Department of Energy under Contract No. DE-AC02-05CH11231. The authors thank the Pohang Accelerator Laboratory (PAL) for the help in GIXRD measurements.

References

1 T. Tanaka, S. –T. Sun, Y. Hirokawa, S. Katayama, J. Kucera, Y. Hirose, T. Amiya, *Nature*, 1987, **325**, 796-798.
2 N. Bowden, S. Brittain, A. G. Evans, J. W. Hutchinson, G. M. Whitesides, *Nature*, 1998, **393**, 146-149.
3 Y. Klein, E. Efrati, E. Sharon, Science, 2007, 315, 1116-1120.
4 E. P. Chan, E. J. Smith, R. C. Hayward, A. J. Crosby, *Adv. Mater.*, 2008, **20**, 711-716.
5 S. Vajpayee, K. Khare, S. Yang, C. –Y. Hui, A. Jagota, *Adv. Funct. Mater.*, 2011, **21**, 547-555.
6 C. S. Davis, D. Martina, C. Creton, A. Lindner, A. J. Crosby, *Langmuir*, 2012, **28**, 14899-14908.
7 J. Y. Chung, J. P. Youngblood, C. M. Stafford, *Soft Matter*, 2007, **3**, 1163-1169.
8 K. Khare, J. Zhou, S. Yang, Langmuir, 2009, 25, 12794-12799.
9 J. D. Pegan, A. Y. Ho, M. Bachman, M. Khine, *Lab Chip*, 2013, **13**, 4205-4209.
10 S. M. Woo, C. M. Gabardo, L. Soleymani, *Anal. Chem.*, 2014, **86**, 12341-12347.
11 J. B. Kim, P. Kim, N. C. Pégard, S. J. Oh, C. R. Kagan, J. W. Fleischer, H. A. Stone, Y. –L. Loo, *Nat. Photonics*, 2012, **6**, 327-332.
12 J. Moon, E. Kim, S. K. Park, K. Lee, J. –W. Shin, D. –H. Cho, J. Lee, C. W. Joo, N. S. Cho, J. –H. Han, B. –G. Yu, S. Yoo, J. –I. Lee, *Org. Electron.*, 2015, **26**, 273-278.
13 S. G. Lee, H. Kim, H. H. Choi, H. Bong, Y. D. Park, W. H. Lee, K. Cho, *Adv. Mater.*, 2013, **25**, 2162-2166.
14 B. H. Kim, Y. Choi, J. Y. Kim, H. Shin, S. Kim, S. W. Son, S. O. Kim, P. Kim, *Adv. Mater.*, 2014, **26**, 4665-4670.
15 U. N. Maiti, W. J. Lee, J. M. Lee, Y. Oh, J. Y. Kim, J. E. Kim, J. Shim, T. H. Han, S. O. Kim, *Adv. Mater.*, 2014, **26**, 40-67.
16 D. J. Li, U. N. Maiti, J. Lim, D. S. Choi, W. J. Lee, Y. Oh, G. Y. Lee, S. O. Kim, *Nano Lett.*, 2014, **14**, 1228-1233.
17 K. E. Lee, S. P. Sasikala, H. J. Lee, G. Y. Lee, S. H. Koo, T. Yun, H. J. Jung, I. H. Kim, S. O. Kim, *Part. Part. Syst. Charact.*, 2017, **34**, 1600375.
18 J. Leem, M. C. Wang, P. Kang, S. Nam, *Nano Lett.*, 2015, **15**, 7684-7690.
19 P. Kang, M. C. Wang, P. M. Knapp, S. Nam, *Adv. Mater.*, 2016, **28**, 4639-4645.
20 J. Zang, C. Cao, Y. Feng, J. Liu, X. Zhao, *Sci. Rep.*, 2014, **4**, 6492.
21 S. J. Kim, D. W. Kim, J. Lim, S. Y. Cho, S. O. Kim, H. –T. Jung, *ACS Appl. Mater. Interfaces*, 2016, **8**, 13512-13519.
22 F. Zou, H. Zhou, D. Y. Jeong, J. Kwon, S. U. Eom, T. J. Park, S. W. Hong, J. Lee, *ACS Appl. Mater. Interfaces*, 2017, **9**, 1343-1351.
23 Y. Liu, Kenry, Y. Guo, S. Sonam, S. K. Hong, M. H. Nai, C. T. Nai, L. Gao, J. Chen, B. J. Cho, C. T. Lim, W. Guo, K. P. Loh, *Adv. Funct. Mater.*, 2015, **25**, 5492-5503.
24 W. K. Lee, J. Kang, K. S. Chen, C. J. Engel, W. B. Jung, D. Rhee, M. C. Hersam, T. W. Odom, *Nano Lett.*, 2016, **16**, 7121-7127.
25 P. Y. Chen, J. Sodhi, Y. Qui, T. M. Valentin, R. S. Steinberg, Z. Wang, R. H. Hurt, I. Y. Wong, *Adv. Mater.*, 2016, **28**, 3564-3571.
26 P. Y. Chen, M. Liu, Z. Wang, R. H. Hurt, I. Y. Wong, *Adv. Mater.*, 2017, **29**, 1605096.
27 W. Chen, X. Gui, B. Liang, M. Liu, Z. Lin, Y. Zhu, Z. Tang, *ACS Appl. Mater. Interfaces*, 2016, **8**, 10977-10984.
28 J. Choi, H. J. Kim, M. C. Wang, J. Leem, W. P. King, S. Nam, *Nano Lett.*, 2015, **15**, 4525-4531.
29 P. Giannozzi, S. Baroni, N. Bonini, M. Calandra, R. Car, C. Cavazzoni, D. Ceresoli, G. L. Chiarotti, M. Cococcioni, I. Dabo, A. D. Corso, S. de Gironcoli, S. Fabri, G. Fratesi, R. Gebauer, U. Gerstmann, C. Gougoussis, A. Kokali, M. Lazzeri, L. Martin-Samos, N. Marzari, F. Mauri, R. Mazzarello, S. Paolini, A. Pasquarello, L. Paulatto, C. Sbraccia, S. Scandolo, G. Sclauzero, A. P. Seitsonen, A. Smogunov, P. Umari, R. M. Wentzcovitch, *J. Phys.: Condens. Matter*, 2009, **21**, 395502.
30 T. P. M. Goumans, A. Wander, W. A. Brown, C. R. A. Catlow, *Phys. Chem. Chem. Phys.*, 2007, **9**, 2146-2152.
31 H. J. Monkhorst, J. D. Pack, Phys. Rev. B., 1976, 13, 5188-5192.
32 D. W. Kim, Y. H. Kim, H. S. Jeong, H. –T. Jung, *Nat. Nanotechnol.*, 2011, **7**, 29-34.
33 C. J. An, S. J. Kim, H. O. Choi, D. W. Kim, S. W. Jang, M. L. Jin, J. –M. Park, J. K. Choi, H. –T. Jung, *J. Mater. Chem. A*, 2014, **2**, 20474-20480.
34 S. Y. Cho, Y. Lee, H. J. Koh, H. Jung, J. S. Kim, H. W. Yoo, J. Kim, H. –T. Jung, *Adv. Mater.*, 2016, **28**, 7020-7028.
35 A. Castellanos-Gomez, R. Roldan, E. Cappelluti, M. Buscema, F. Guinea, H. S. van der Zant, G. A. Steele, *Nano Lett.*, 2013, **13**, 5361-5366.
36 N. T. Cuong, M. Otani, S. Okada, *Phys. Rev. Lett.*, 2011, **106**, 106801.
37 J. P. Perdew, A. Zunger, *Phys. Rev. B.*, 1981, **23**, 5048-5079.
38 K. Lee, É. D. Murray, L. Kong, B. I. Lundqvist, D. C. Langreth, *Phys. Rev. B.*, 2010, **82**, 081101.
39 Y. Shibuta, J. A. Elliott, *Chem. Phys. Lett.*, 2011, **512**, 146-150.
40 H. O. Kim, D. W. Kim, S. J. Kim, S. B. Yang, H. –T. Jung, *Adv. Mater.*, 2014, **26**, 4575-4581.
41 H. O. Choi, D. W. Kim, S. J. Kim, K. M. Cho, H. –T. Jung, *J. Mater. Chem. C*, 2014, **2**, 5902-5909.
42 Y. P. Hsieh, Y. H. Chu, H. G. Tsai, M. Hoffman, *Nanotechnology*, 2016, **27**, 105602.
43 B. Hu, H. Ago, Y. Ito, K. Kawahara, M. Tsuji, E. Magome, K. Sumitani, N. Mizuta, K. –I. Ikeda, S. Mizuno, *Carbon*, 2012, **50**, 57-65.
44 I. Vlassiouk, S. Smirnov, M. Regmi, S. P. Surwade, N. Srivastava, R. Feenstra, G. Eres, C. Parish, N. Lavrik, P. Datskos, S. Dai, P. Fulvio, *J. Phys. Chem. C*, 2013, **117**, 18919-18926.
45 K. Hayawhi, S. Sato, M. Ikeda, C. Kaneta, N. Yokoyama, *J. Am. Chem. Soc.*, 2012, **134**, 12492-12498.
46 T. Jiang, R. Huang, Y. Zhu, *Adv. Funct. Mater.*, 2014, **24**, 396-402.
47 X. Chen, C. Yi, C. Ke, *Appl. Phys. Lett.*, 2015, **106**, 101907.
48 L. Xiang, S. Y. Ma, F. Wang, K. Zhang, *J. Phys. D: Appl. Phys.*, 2015, **48**, 395305.
49 G. H. Lee, R. C. Cooper, S. J. An, S. lee, A. van der Zande, N. Petrone, A. G. Hammerberg, C. Lee, B. Crawford, W. Oliver, J. W. Kysar, J. Hone, *Science*, 2013, **340**, 1073-1076.

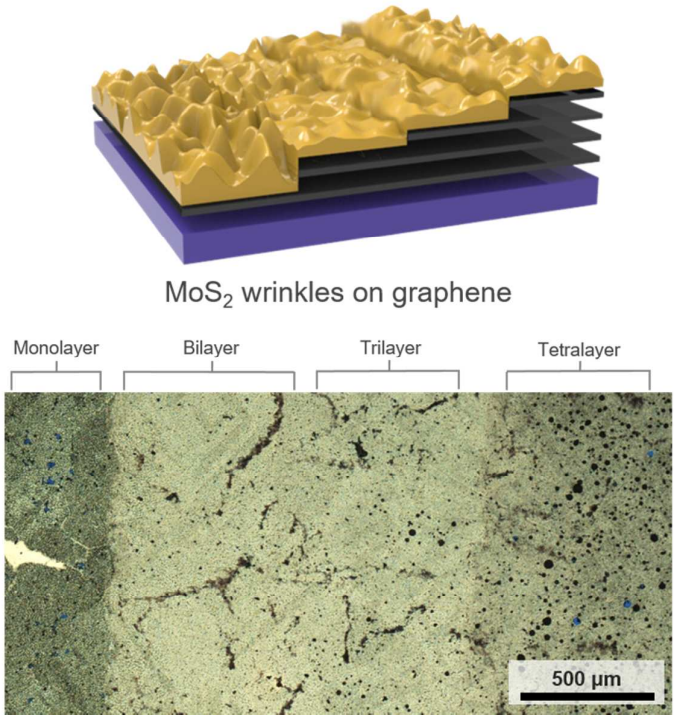

In this work, the influence of the graphene grain structure and thickness on the MoS_2 wrinkle features were investigated.